

Chaotic Scattering

Chaotic dynamics in low dimensional conservative systems is a well established phenomenon and has attracted a great deal of interest during the last decade. Most of this work has been devoted to bounded systems. More recently, however, irregular chaotic phenomena have also been observed and studied for open (scattering) systems. For recent reviews of chaotic scattering, see the articles by Eckhardt [1], Smilansky [2], and Blümel [3]. Chaotic dynamics in such scattering systems is important for many collision processes, e.g., the formation and decay of intermediate collision complexes, the redistribution of energy during a collision and, last but not least, for subsequent processes (such as reactive collision with a third collision partner, the absorption or emission of radiation, etc.), which become more probable the longer the lifetime of the intermediate colliding system.

Scattering systems are, by definition, open systems: the trajectories are not confined to a bounded region. With increasing time, trajectories will leave the interaction region and eventually escape to infinity, where the dynamics can

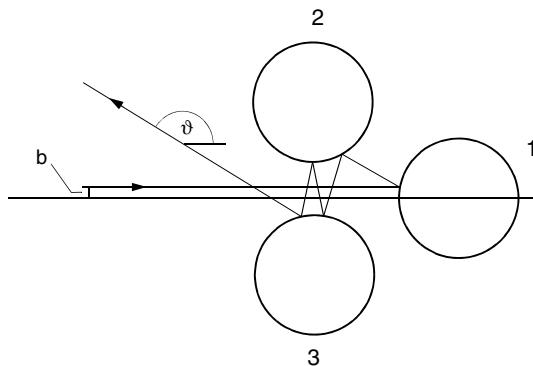


Fig. 6.1. Multiple scattering of a particle off a planar three-disk system forming an equilateral triangle.

be regular. Therefore, the long time limit, which is an essential concept of many rigorous mathematical results of chaotic dynamics, must be treated differently. Let us assume, for simplicity, that we can clearly distinguish between an asymptotic region and a finite scattering zone. Then, most of the scattering trajectories have a finite collision time. To be more precise, for typical systems the set of all scattering trajectories with infinite collision time ('sticking trajectories') is of measure zero. At first sight, this leaves very little room for manifestly chaotic phenomena. Another important set consists of all bounded periodic trajectories. The so-called 'chaotic repeller' [4] is the set of all trajectories which stay trapped for $t \rightarrow \infty$ and contains the two sets mentioned above.

Various systems showing chaotic scattering have been analyzed in detail [1]–[3]. One of the best studied models is the collision of a point mass with three fixed circular disks in a plane, arranged in most cases at the vertices of an equilateral triangle [2, 4, 5]. This system has the advantage of clearly demonstrating several features of classical chaotic scattering without the need for integrating differential equations. The dynamics is of the billiard type, consisting of straight-line segments plus elastic reflection from hard walls. In addition, the dynamics only trivially depends on the energy; in particular, the classical repeller undergoes no structural bifurcations when the energy is varied. This also makes the three-disk system well suited for investigating classical–quantum interrelations [6, 7]. The system has also been used to demonstrate classical chaotic scattering experimentally [8].

The classical disk scattering system in a plane has also been extended to three space dimensions (i.e., to scattering off a cluster of three (and more)

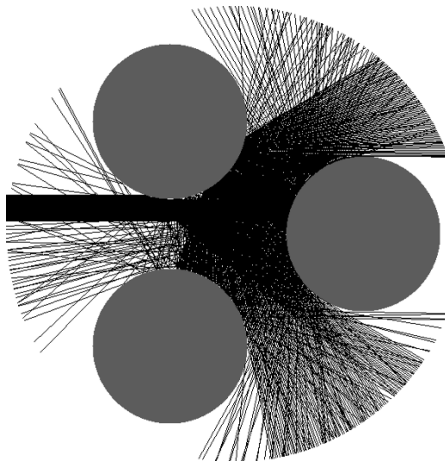


Fig. 6.2. Multiple scattering of a beam of 400 trajectories with impact parameter $1 \leq b \leq 3$. The three disks (radii $r = 6$) form an equilateral triangle with $R = 10$.

hard spheres) by Chen et.al. [9] and Korsch and Wagner [10]. Here, we will confine ourselves to the two-dimensional case.

6.1 Scattering off Three Disks

This planar model for chaotic scattering consists of a cluster of three hard circular disks $i = 1, 2, 3$ with radii r_i at distances R_i from a center at angular positions φ_i measured with respect to the horizontal scattering axis. A point mass impinging from the left with impact parameter b undergoes multiple elastic reflections from the disks and, after a number of n collisions, escapes finally with scattering angle ϑ . It is useful to note that the same system can also be interpreted as the reflection of parallel light rays from an arrangement of three perfectly reflecting disks.

Figure 6.1 illustrates the geometry of the system for the case of three disks with the same radii $r_i = r$ and having the same distances $R_i = R$ ($i = 1, 2, 3$) and forming an equilateral triangle oriented symmetrically with respect to the scattering axis. In this configuration, the distance between the centers of the disks is $L = R\sqrt{3}$.

In Fig. 6.2, the complex dynamics of the three-disk system is illustrated. A beam of 1000 trajectories in the impact parameter interval $0.5 \leq b \leq 3.0$ is displayed for a disk of radius $r = 6$ ($R = 10$), which is analyzed in more detail below. Figure 6.3 shows the collision number, i.e., the number n of impacts which occur before the scattered particle escapes. This is a measure of the lifetime of the collision complex. Also shown is the deflection function, i.e.,

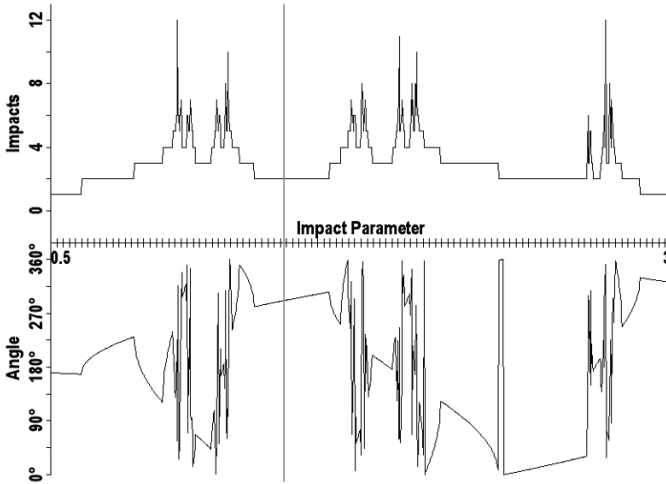


Fig. 6.3. Collision number $n(b)$ and scattering angle $\vartheta(b)$ as a function of the impact parameter b for $r = 6$ and $R = 10$.

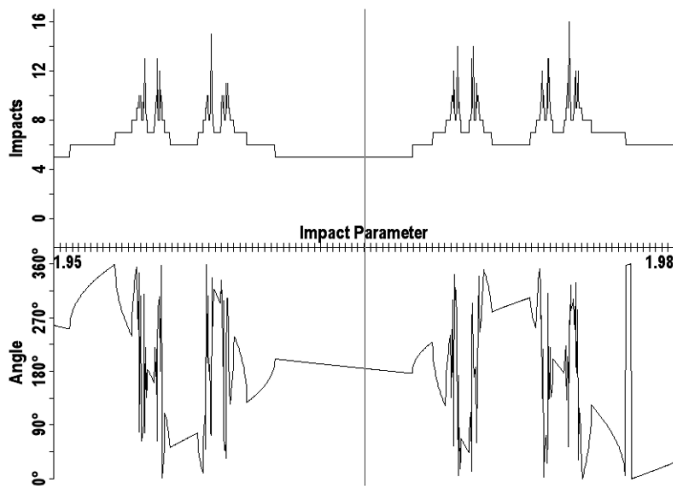


Fig. 6.4. Magnification of the impact parameter interval $1.95 \leq b \leq 1.98$ for $r = 6$ and $R = 10$.

the scattering angle ϑ (modulo π), as a function of the impact parameter b . A magnification of the figure for the interval $1.95 \leq b \leq 1.98$ is shown in Fig. 6.4, and we see a picture almost identical to Fig. 6.3.

By increasing the value of r , the dynamics becomes more and more complicated. Fig. 6.5 shows the collision number and scattering angle in the impact parameter interval $0.5 \leq b \leq 1.0$ for $r = 8$. Again, magnification of the interval $0.673 \leq b \leq 0.698$ shown in Fig. 6.6 shows no smoothing of these functions. The apparent self-similarity demonstrated in these figures continues under repeated magnification, revealing a fractal structure of the dynamics which can be measured by its fractal dimension d (see computer experiment 6.4.4). The maximum value of the collision number observed in an equidistant scan of an impact parameter interval increases under magnification, and approaches infinity as one gets closer and closer to the chaotic repeller. The dynamics is extremely sensitive to the initial conditions, a feature characteristic of chaotic dynamics.

The collision number shows discontinuities at certain impact parameters; the deflection function is continuous and its first derivative is discontinuous at the same set of impact parameters. The trajectories in the interval between these discontinuities can be characterized by the same collision sequence, for example the orbit shown in Fig. 6.1 is described by the sequence $1 \rightarrow 2 \rightarrow 3 \rightarrow 2 \rightarrow 3$, where 1, 2, 3 are the numbers of the disks. A trajectory can not hit the same disk twice in direct succession and, therefore, the collision sequence can even be coded binarily, suggesting a treatment by symbolic dynamics [5, 4]. We associate with a sequence of two collisions in a positive cyclic direction ($1 \rightarrow 2$, $2 \rightarrow 3$, or $3 \rightarrow 1$) the symbol ‘1’, otherwise a ‘0’. The sequence of

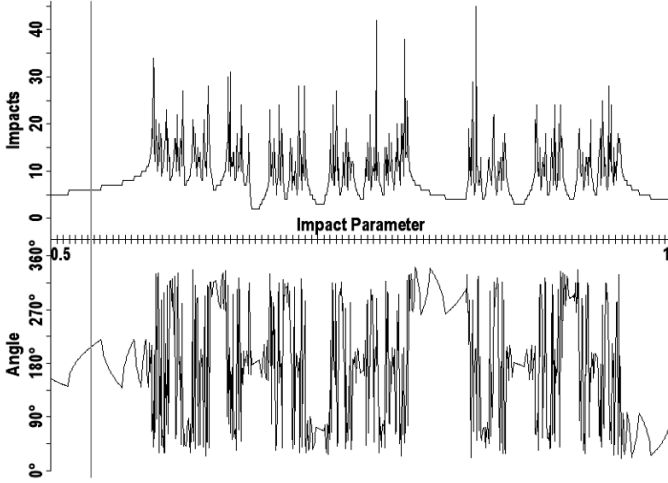


Fig. 6.5. Collision number $n(b)$ and scattering angle $\vartheta(b)$ as a function of the impact parameter b for $r = 8$, $R = 10$.

collisions of Fig. 6.1 is then given by ‘1101’. At the boundary of an interval of continuity, the trajectory becomes tangential to one of the disks and changes the dynamics discontinuously by hitting another disk. This set of tangential trajectories organizes the structure of the trajectory set. For small values of r , there is a one-to-one relationship between all binary sequences and the topologically different trajectories [5]. If r is large, the disks get more and more hidden by each other and some collision sequences become dynamically forbidden. A simple geometrical consideration shows that, for

$$0 \leq r/R \leq 3/4, \quad (6.1)$$

no path between two disks can be affected by the third one, i.e., these screening effects are unimportant for trajectories which collide with more than two disks. In addition, there are outer screening effects, because a disk can hide a part of another disk, i.e., it is partly invisible from the direction of impact. This hidden part can be made visible by changing the impact direction, in contrast to the inner screening effects discussed above.

The dynamics shows an almost self-similar structure, as illustrated by Figs. 6.3 to 6.6. The set of singularities — the set of all impact parameters leading to trapped trajectories — is a fractal. In one dimension, the fractal dimension d of a set measures the asymptotic scaling of the number N of intervals of size ϵ needed to cover the set:

$$N(\epsilon) \sim \epsilon^{-d} \quad \text{for } \epsilon \rightarrow 0. \quad (6.2)$$

For a self-similar set, invariant under a transformation ‘restriction of the set onto a fraction $1/m$ of the set followed by a magnification by a scale factor

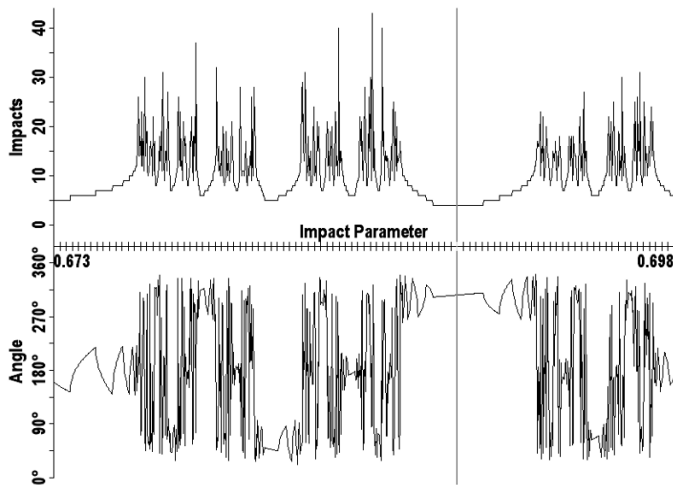


Fig. 6.6. Magnification of the impact parameter interval $0.673 \leq b \leq 0.698$ for $r = 8$, $R = 10$.

s' , (6.2) simplifies to

$$d = \frac{\ln m}{\ln s}. \quad (6.3)$$

The most famous fractal set is the Cantor set, more precisely the ‘1/3 Cantor set’, which is constructed by erasing the middle 1/3 of a unit interval and iterating this procedure for the subintervals. After n such erasing processes, we have 2^n intervals of length $(1/3)^n$ and the total measure of the remaining set is $(2/3)^n$, which goes to zero for $n \rightarrow \infty$, i.e., the limiting Cantor set is of measure zero. Alternatively, one can label two intervals of generation $n = 1$ by ‘0’ and ‘1’, the daughter generation of ‘0’ as an additional ‘0’ or ‘1’, i.e., as ‘00’ and ‘01’, and those of ‘1’ as ‘10’ and ‘11’. Continuing this process shows that the Cantor set is uniquely labeled by the sequences of ‘1’s and ‘0’s in the form ‘0110101...’, which are the binarily coded real numbers between zero and one. This correspondence is one-to-one, i.e., the ‘1/3 Cantor set’ is not countable. Furthermore, it is nowhere dense. The last two attributes are used to define more general Cantor sets.

The ‘1/3’ Cantor set is self-similar under reduction to 1/2 of the set and magnification by a factor $s = 3$. Its fractal dimension is therefore

$$d = \frac{\ln 2}{\ln 3} = 0.6309. \quad (6.4)$$

The fractal dimension of sets observed in the dynamics can be used as a quantitative measure of the chaoticity. A fractal of the three-disk scattering function will be analyzed in the computer experiments described in Sec. 6.4.4.

6.2 Numerical Techniques

Numerically, the problem is very simple and, of course, similar to the closed billiards studied in Chap. 3. The trajectory is (piecewise) a straight-line. The program computes the intersections of this line with the three fixed disks. We obtain six or fewer intersection points. The one at minimum distance to the position of the projectile is the position of the next impact. A line is drawn between the last position of the particle and the new one. Let us assume that a collision with disk i will occur. Then, the angle between the particle trajectory and the radius vector from the position of the center of the disk i to the collision point is computed, and the reflection law determines the direction of the particle after collision. This procedure is repeated until no collision is found and the projectile escapes to infinity. Then, the scattering angle and the collision number are determined and stored. The program also displays the collision sequence, coded as described above.

The program also allows computation of the fractal dimension (6.2). Instead of using the definition directly, we adopt a technique which can be used for fractal sets given as a limiting set of ‘generations’ n for $n \rightarrow \infty$, where each generation is the reduction of the set to $1/m$ th of the previous set. A scaling factor s^{-1} is, however, not sharply defined. When A_n is the total measure of generation n , it can be covered by $N(\epsilon_n) \sim \epsilon^{-d}$ intervals of size $\epsilon = A_n m^{-n}$ and we find

$$A_n = \epsilon_n N(\epsilon_n) \sim \epsilon^{1-d} = (A_n m^{-n})^{1-d} \quad (6.5)$$

and, hence, the A_n will decrease exponentially for large n

$$A_n \sim m^{-n(1/d-1)} = e^{-\gamma n} \quad (6.6)$$

with rate

$$\gamma = (1/d - 1) \ln m. \quad (6.7)$$

We end up with

$$d = \frac{\ln m}{\ln m + \gamma} = \frac{\ln m}{\ln(m\delta)}, \quad (6.8)$$

where

$$\delta = e^\gamma \approx \delta_n = \frac{A_{n-1}}{A_n} \quad (6.9)$$

is approximately the ratio between the measure of two successive generations. For a self-similar set with scaling factor s we have $A_n = mA_{n-1}/s$, and we recover the result (6.3).

6.3 Interacting with the Program

Starting the program 3DISK displays the *Main Menu* together with a single trajectory scattered from the three disks as shown in Fig. 6.7. Also shown is

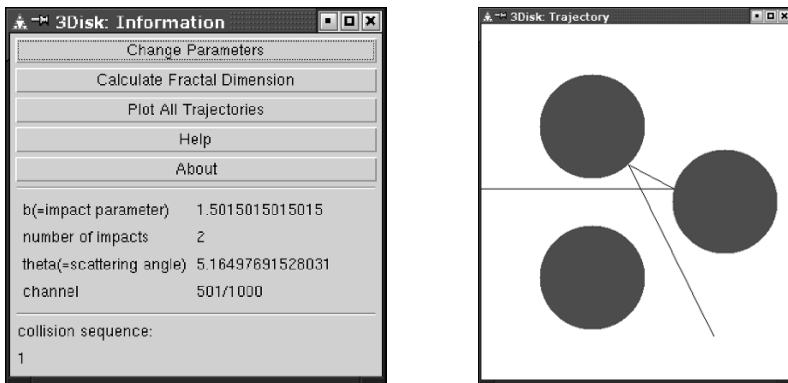


Fig. 6.7. Main menu of program 3DISK as well as a trajectory for the preset conditions.

the collision number $n(b)$ and the scattering angle $\vartheta(b)$ as a function of the impact parameter b for the preset parameters (see Fig. 6.8).

Main Menu

Here, the user can select the range of impact parameters, choose the mode of representation, change the radii of the disks and activate the simulation.

- **Change Parameters** — In the window shown in Fig. 6.9 the range of impact parameters $b_1 \leq b \leq b_2$ at

$$b^\nu = b_1 + (b_2 - b_1)(\nu - 1)/(N - 1), \quad \nu = 1, \dots, N \quad (6.10)$$

can be chosen, as well as the number N of calculated samples (also denoted as the channel number). One can also change the radii of the three disks as well as their positions. Initially all disks have radius six and are placed at a distance of 10 from the origin forming an equilateral triangle.

- **Calculate Fractal Dimension** — The fractal dimension of the set of trapped trajectories is calculated as described in Sect. 6.2 (see also the numerical experiment in Sect. 6.4.4).
- **Plot All Trajectories** — All calculated trajectories are displayed.
- **Help** — provides online information on the program.

By mouse clicking in the scattering diagrams, the details of the corresponding trajectory are displayed in the lower part of the menu window, namely impact parameter, collision number (i.e., the total number of impacts), scattering angle, and the channel number (the index of the selected impact parameter in the array of computed ones). In addition, the collision sequence is listed.

A new impact parameter interval can be selected by zooming in or out. Start zooming in by pressing the <+>-key and move the cursor to the lower

boundary of the impact parameter interval you want to magnify. Hold the mouse button pressed, move the mouse to the upper boundary, and release the mouse button.

Hot Keys in the program 3DISK:

Keys in the *Trajectory-Window* :

<Space> : iterate the trajectory stepwise

<Return> : plot the whole trajectory

Keys in the *Scattering-Diagram* window:

<+> : zoom in

<-> : zoom out

<z> : zooming in using the channel number

<l>,<left> : next impact parameter to the left

<r>,<right> : next impact parameter to the right

<page down> : move 10 impact parameters left

<page up> : move 10 impact parameters right

Keys in both windows:

<F2>,<s> : save picture

Remarks: Due to the extreme sensibility of the scattering to the initial conditions, the scattering diagram or the fractal dimension varies wildly when

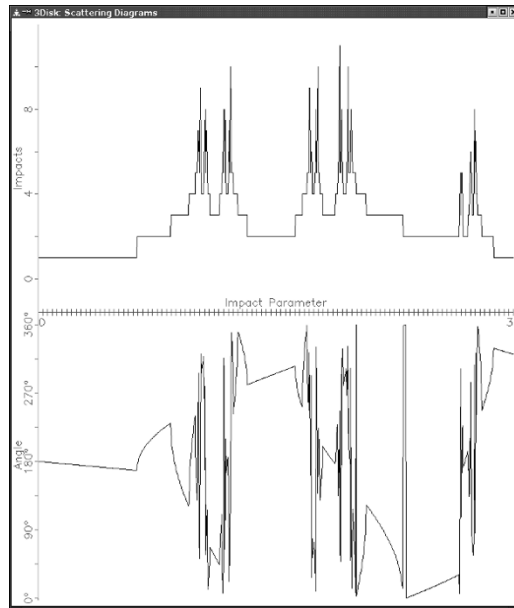


Fig. 6.8. Collision number $n(b)$ and scattering angle $\vartheta(b)$ as a function of the impact parameter b for the preset parameters.

one changes the number of calculated rays even just slightly. This effect increases when zooming in. The same applies to the displayed interval of impact parameters.

6.4 Computer Experiments

6.4.1 Scattering Functions and Two-Disk Collisions

For the case where a point particle collides with a single disk (radius r), the deflection function is given by

$$\vartheta = 2 \cos^{-1}(b/r), \quad (6.11)$$

where the impact parameter b is measured with respect to the center of the disk. It is instructive to study first the deflection function for a single disk numerically (e.g., by changing the radii in the preset set-up to $r_1 = 4$ and $r_2 = r_3 = 0$ in the impact parameter region $0 < b < 12$), which shows the functional dependence (6.11). The collision number n is equal to one if the particle collides with the disk, and zero otherwise. Increasing now the radius of disk 2 to $r_2 = 1$, we observe various changes in the scattering functions $\vartheta(b)$ and $n(b)$ (see Fig. 6.10):

1. In the large impact parameter region, a second scattering structure, which is due to a first collision with disk 2, appears.

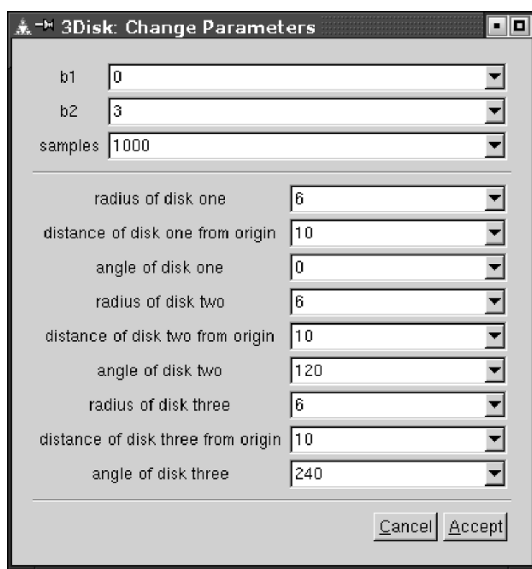


Fig. 6.9. Parameter menu of program 3DISK.

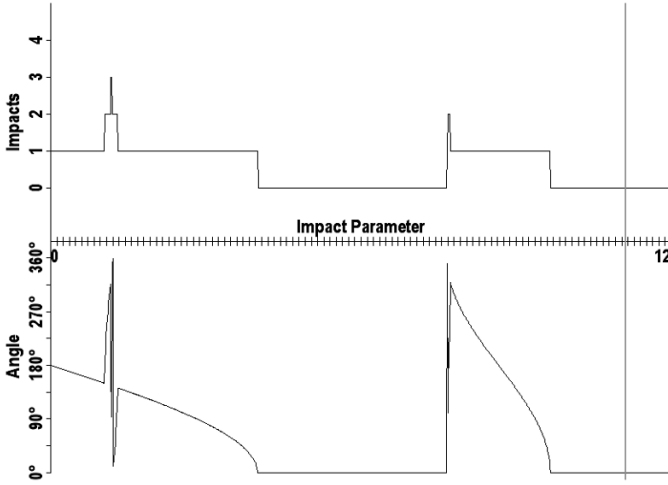


Fig. 6.10. Collision number $n(b)$ and scattering angle $\vartheta(b)$ as a function of the impact parameter b for two disks with radii $r_1 = 4$ and $r_2 = 1$ ($R = 10$).

2. In the small impact parameter region, the deflection function is distorted due to trajectories hitting first disk 1 and then disk 2. This new region is located at the angular position of the center of disk 2 seen from disk 1, i.e., at $\vartheta = 150^\circ$ with angular width $\Delta\vartheta \approx 2r_2/L$. The region is bounded by rays tangential to disk 2. A central ray in this region is a radial ray of disk 2, which is therefore reflected backward with an overall scattering angle $\vartheta = 180^\circ$ (see Fig. 6.11). One can numerically locate this ray at an impact parameter $b = 1.1646653$. The collision number increases by at least one in this region.
3. The additional deflection angle caused by the second collision with disk 2 varies over 360° . Therefore, a subinterval of these rays must hit disk 1 once again, giving rise to a new substructure where the collision number again increases by one. This procedure can be continued. In this region,

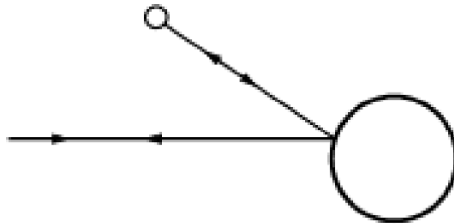


Fig. 6.11. Radial ray with backward reflection in the center of the double collision region (radii $r_1 = 4$ and $r_2 = 1$; $R = 10$).

there exists an unique ray showing infinitely many reflections (a so-called ‘sticking trajectory’), which can be found at $b = 1.16914770328$.

4. The same behavior is found in the large impact parameter region.

Let us interpret these findings in the language of optics, considering the reflection of parallel light rays from two circular mirrors (the two disks). We will observe a mirror image of disk 2 in mirror 1, and vice versa. The image of 2 therefore contains an image of disk 1, which carries an image of disk 2, and so on. We find in each disk a nested sequence of repeated mirror images, which converges to a point. The two rays centered at these points are the two long-lived sticking trajectories.

Alternatively, one can start from a periodic orbit consisting of a radial trajectory (or ray) along the line between the centers of the two disks. This trajectory is a periodic two-bounce orbit which is unstable, i.e., any small perturbation will lead to a trajectory which moves away from this orbit, and eventually escapes to infinity. The sticking trajectory is such a path in the reverse direction, where the ray comes arbitrarily close to the unstable periodic orbit after infinite time. More precisely, it is an element of the stable manifold of an unstable fixed point, the periodic orbit.

More details regarding two-disk scattering, e.g., explicit formulae for minimum and maximum collision angles, collision mappings, and the location of the trapped orbits can be found in Ref. [11].

In the two-disk case, there is only one unstable periodic orbit and no chaotic scattering, since the repeller consists only of this orbit and, hence, has no fractal structure. The two-disk organization of the collision dynamics

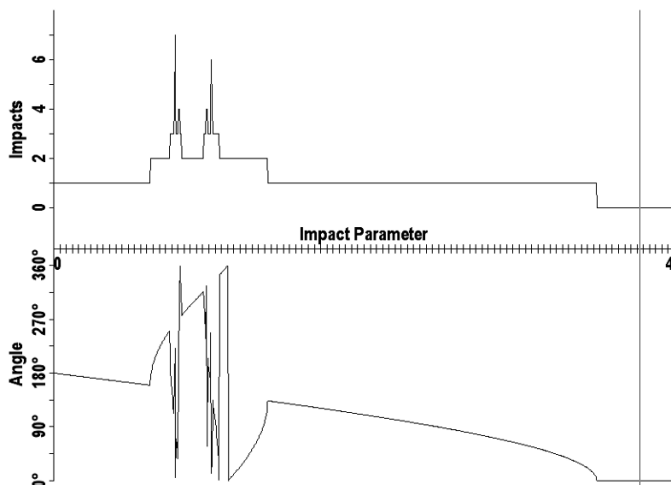


Fig. 6.12. Collision number $n(b)$ and scattering angle $\vartheta(b)$ as a function of the impact parameter b for three disks with radii $r = 3.5$ and $R = 10$ in the impact parameter range $0 \leq b \leq 4$.

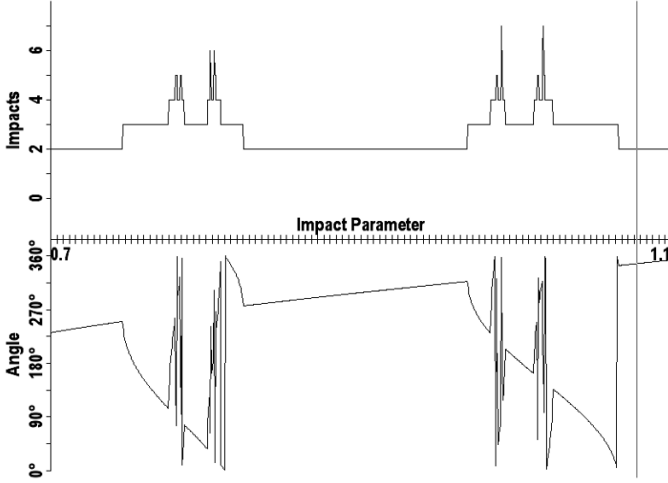


Fig. 6.13. Magnification of Fig. 6.12 in the impact parameter range $0.7 \leq b \leq 1.1$.

will, however, reappear as a substructure in the three-disk case, where the collision dynamics will turn out to be chaotic. This is studied below.

6.4.2 Tree Organization of Three-Disk Collisions

Here, we will explore the organization of three-disk scattering in more detail. Let us start with relatively small disks with the same radius $r = 3.5$ placed again on an equilateral triangle at distance $R = 10$ from the center, where disk 1 is placed at $\theta = 0^0$ (preset configuration).

Figure 6.12 shows the collision function in the impact parameter range $0 \leq b \leq 4$, which is sampled by 1000 trajectories with equidistant impact parameters (preset case). We note that all trajectories in the range $0 \leq b \leq 3.5$ collide first with disk 1. On top of the $n = 1$ plateau, we see two ‘chimneys’ of the first daughter generation with $n \geq 2$. A magnification of the interval $0.7 \leq b \leq 1.1$ in Fig. 6.13 — again with 1000 trajectories — reveals further chimneys on top of the previous ones and so on, as discussed above. Let us now go into more detail by looking at the sequence of collisions in the different regions. This sequence is coded by a sequence of ‘1’s or ‘0’s, where ‘1’ stands for a collision with disk $i + 1$, 0 for a collision with disk $i - 1$, when the last collision occurred with disk i ($i = 1, 2, 3$ modulo 3).

After recomputing the results shown in Fig. 6.13, one can move one of the vertical lines to a point of interest by means of the cursor. The corresponding sequence of collisions is displayed in the window *3Disk: Information*.

Key (S) activates the display of the sequence of collisions. One can easily check that the whole plateau with $n = 2$ yields a sequence of collisions consisting only of a ‘1’, i.e., a collision with disk 2 after the first collision with disk 1.

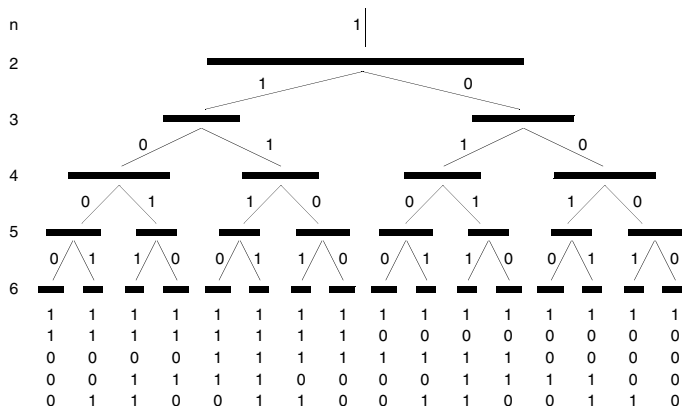


Fig. 6.14. Tree-structure of the organization of the sequences of collisions.

The two subplateaus with $n = 3$ yield a sequence ‘11’ for the left, and ‘10’ for the right subplateau. Translating to the ‘real’ trajectory, this is a third collision with disk 3 or 1, respectively. The two subplateaus have different sizes Δb ; the smaller one appears to the left. The angular width of the plateaus is, however, the same, namely $\Delta\vartheta \approx 0.15\pi$.

Exploring the $n = 4$ generation, we find two subintervals of the left $n = 3$ plateau (symbolic code ‘110’ and ‘111’ from left to right), and two of the right one (symbolic code ‘100’ and ‘101’). In both cases, the outer interval (the one closer to the boundary of the parent generation $n = 3$) is the larger one.

This scheme is repeated in the following generations. Figure 6.14 shows the organization schematically as a tree diagram. The different plateaus are shown as a function of the impact parameter b (not properly scaled!). The binary code for each interval can be read directly from the diagram by collecting the 1s and 0s following the different branches. The codes for generation $n = 6$ are, e.g., ‘11010’, ‘11011’, ‘11000’, etc.

The 2^{n-1} plateaus for generation n (note that Fig. 6.14 only gives the tree for the 2^{n-2} sequences starting with ‘1’) can be uniquely labeled by the collision sequences with length $n-1$, and vice versa. There is a one-to-one mapping between the sequences of collisions and the plateaus of the collision function $n(b)$, and the whole scheme of construction closely resembles the Cantor set structure discussed above. In order to localize numerically a trajectory interval with a prescribed sequence of collisions one can start by simply localizing the plateau which reproduces the first few digits of the sequence. Then, by repeated magnification, one can find the subintervals which satisfy the next digits. A selection between two different subintervals is required in each step.

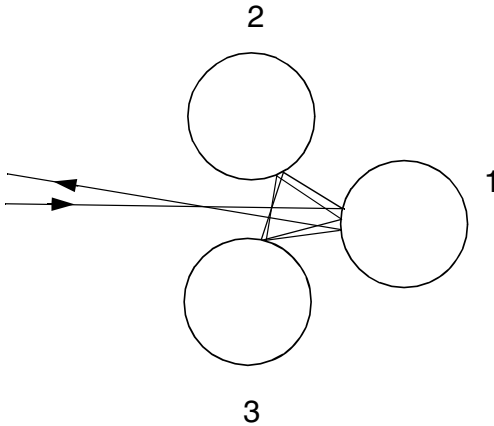


Fig. 6.15. Long-lived trajectory approximately following a triangular periodic orbit for several periods ($r = 0.35$, $R = 10$).

6.4.3 Unstable Periodic Orbits

A sticking trajectory never escapes from the scattering region and the collision sequence for such a trajectory will never terminate. Thus, these trajectories are exactly those with an infinite collision sequence. The set of all sticking trajectories forms a Cantor set of measure zero. A countable subset of these sticking trajectories are those coming infinitely close to an unstable periodic orbit. In the binary code, they appear as sequences ending up in a periodic tail. Trajectories with impact parameters close to such a sticking trajectory are attracted by the periodic orbit, and follow it for a while until they are finally repelled. Figure 6.15 shows an orbit attracted and repelled by the period-three orbit forming an equilateral triangle (binary code ‘11111...’).

Further periodic trajectories — more precisely, impact parameters of trajectories approaching an unstable periodic orbit — are numerically localized by the method described above and shown in Fig. 6.16 for the preset configuration (disk radii $r = 6.00001$ (for historical reasons¹) and $R = 10$). The

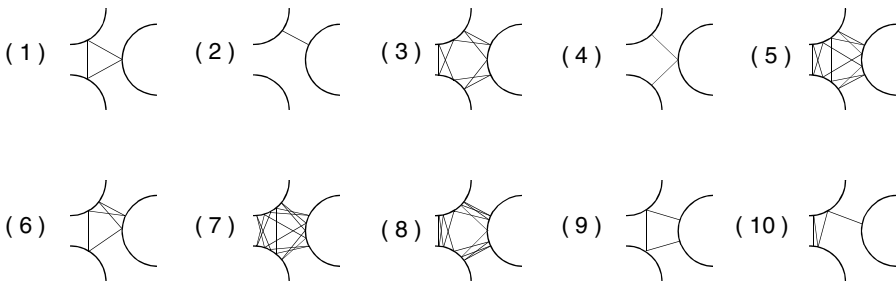


Fig. 6.16. Unstable periodic orbits.

¹In previous editions of this book, the programs used a small disk of radius 0.00001 instead of a point mass.

data of these orbits are listed in Table 6.1. Theoretically, such an orbit can be localized with arbitrary precision. In practice, however, one is limited by the finite number of digits and the collision sequence is finite. The maximum collision number $n(b)$ is also listed in the table. In the symbolic code of the unstable orbit, a primitive period is marked by a dot. Periodicity of the trajectory requires that the number of zeros and ones in the symbolic code be equal (modulo three). If this is not the case, the primitive period must be repeated until this condition is met, and the true period is three times longer than the symbolic period.

The periodic trajectories in Table 6.1 are ordered with respect to the length of their symbolic period. It should be noted that the table is *not* complete. As an exercise, one can find the missing orbits with symbolic code ‘111110’, ‘111100’, and ‘111010’. It is also possible to extend the list and locate orbits with higher period.

Let us point out some features characteristic of periodic orbits (compare the related discussion for the gravitational wedge billiard in Sect. 4.3.1):

- There are orbits with a threefold symmetry in space (examples (1), (3), (5), (7), and (8) in Fig. 6.16 and Table 6.1). These orbits perform a full rotation in space with respect to the center in the triangular disk configuration. It should be noted that there also exist duplicates of these orbits, transversed in the inverse direction, i.e., the ‘1’s and ‘0’s are interchanged in the binary code.
- If an orbit contains a central ray orthogonal to a disk (examples (2), (4), and (9)), it is simply reflected onto itself. This implies that the binary code is invariant against a reflection, interchanging ‘1’s and ‘0’s at some

Table 6.1. Trajectories approaching unstable periodic orbits with given collision sequence and period p_s . A sequence of period p is marked by upper dots. The period p of the true orbit is equal to p_s or $3p_s$.

	b	$n(b)$		p_s	p
(1)	1.17754799767000	28	... $\dot{1}$ 111111111... $\dot{1}$	1	3
(2)	1.97534632642241	31	... $\dot{1}$ 010101010... $\dot{1}$	2	2
(3)	1.02459608527742	30	... $\dot{1}$ 101101101... $\dot{1}$	3	9
(4)	1.72455696933076	27	... $\dot{1}$ 001100110... $\dot{1}$	4	4
(5)	1.21335412735471	30	... $\dot{1}$ 110111011... $\dot{1}$	4	12
(6)	1.16957287517956	28	... $\dot{1}$ 111011110... $\dot{1}$	5	5
(7)	1.20434893507372	26	... $\dot{1}$ 110011100... $\dot{1}$	5	15
(8)	1.01164038132856	28	... $\dot{1}$ 101011010... $\dot{1}$	5	15
(9)	1.20627203056642	26	... $\dot{1}$ 110001110... $\dot{1}$	6	6
(10)	1.01080193668915	29	... $\dot{1}$ 101010011... $\dot{1}$	8	8

point. It is also evident that there must be exactly two such orthogonal points, or none.

- The orbits which are *not* three-fold symmetric appear three times, because the two rotated orbits are also allowed trajectories. They have the same collision sequence, starting, however, on a disk different from disk number one.
- Orbits (1)–(9) show a reflection symmetry with respect to a symmetry line. This is, of course, not necessarily the case and orbit (10) does *not* show such a symmetry.

The number of periodic orbits shows an exponential proliferation with increasing period. As an exercise, one can try to work out an analytic formula for this number.

6.4.4 Fractal Singularity Structure

In the examples shown above, collision functions have been computed for equilateral triangle configurations with $R = 10$ and disk radii $r = 3.5, 6.0$, and 8.0 . The character of the observed structures in the collision functions was found to be strongly dependent on the radii of the disks. For small disks we have rather clumsy structures ('chimneys' on flat roof tops for $r = 3.5$). For larger disks the structures become finer ('cathedral towers' for $r = 6$) and more and more ragged in the limit of disks touching each other (compare Figs. 6.5 and 6.6 for $r = 8$). This different impressions can be quantitatively expressed in terms of the fractal dimension, as discussed above.

Let us first look at the scaling behavior of the width of the Δb plateaus. The following technique can be used: we compute a series of magnifications following a certain structure, e.g., the larger plateaus shown in Figs. 6.12 and 6.13 for $r = 3.5$ and $R = 10$. Using always the same resolution of, e.g., 10000 computed impact parameters in each plot, we move the vertical line to the lower and upper boundary of the Δb plateau, read the relative coordinates of the boundaries displayed on the screen, and compute the difference. By pressing the **z**-key and entering the relative coordinates, a magnification of this plateau is computed. Again we move the cursor to the next plateau, measure its boundary coordinates once more, and so on. Table 6.2 lists the results when the large plateau is traced in generations $n = 3$ to $n = 9$ starting with an interval $0.5 \leq b \leq 1.5$. Both the length and coordinate of the interval apparently converge and we find a scaling factor between subsequent generations of $s = 10000/1287 = 7.7700$. Assuming self-similarity with this scaling factor formula (6.3) yields a fractal dimension of $d = \ln 2 / \ln s = 0.3381$ (evidently we have $m = 2$). We can, however, also trace the smaller plateau. From Fig. 6.14 we see that, in this case, we follow the '1111...' orbit instead of the '101010...' in the case of the larger interval. The results are also listed in Table 6.2. The scaling factor is $s = 10000/1073 = 9.3197$ and, therefore,

Table 6.2. Width Δb of $n(b)$ plateaus for a sequence of magnifications, following the larger or smaller interval ($r = 3.5$, $R = 10$). Values of b are given as relative coordinates, where the width of the parent interval is always set to 10000.

n	large plateau			small plateau		
	b_{\max}	b_{\min}	Δb	b_{\max}	b_{\min}	Δb
3	4598	5878	1280	1661	2683	1022
4	4397	5685	1288	7057	8138	1081
5	4363	5650	1287	1836	2907	1071
6	4358	5645	1287	7090	8163	1073
7	4359	5646	1287	1836	2908	1072
8	4355	5642	1287	7092	8165	1073
9	4356	5643	1287	1836	2909	1073

a self-similar fractal dimension would be equal to $d = 0.3105$. Assuming a multiscale fractal [12] with two scales $s_1 = 7.7700$ and $s_2 = 9.3197$, one can derive a fractal dimension from the implicit equation

$$s_1^{-d} + s_2^{-d} = 1 \quad (6.12)$$

which yields $d = 0.3239$, which is close to the fractal dimension $d = 0.3231$ computed from the average of the two scaling factors $\bar{s} = (s_1 + s_2)/2 = 8.5448$.

It has already been noted that the hard disk collisions can also be interpreted as mirror images in a perfectly reflecting circular mirror, or a sphere in three dimensions. The imaging properties of such spheres have been analyzed by Berry [13]. Here, we need the lateral reduction of an image, which is approximately

$$s = \left[2(\sqrt{3}R/r - 1) \right]^{-1} \quad (6.13)$$

for large angle scattering [10]. Using this as an approximate average scaling ratio in expression (6.3), for the fractal dimension we obtain [10]

$$d = \frac{\ln 2}{\ln 2(\sqrt{3}R/r - 1)}, \quad (6.14)$$

which reduces to zero in the limit $r \rightarrow 0$ and to unity for $r = \sqrt{3}R/2$, i.e., for disks in contact with each other. For the case of $r/R = 0.35$ considered above, (6.1) yields $d = 0.335$.

Let us now use directly the implemented program feature for calculating the fractal dimension. Computing a (magnified) collision function and pressing *Calculate Fractal Dimension* generates a listing of the measures A_{n-1} and A_n versus n , as well as the approximate fractal dimension calculated from (6.8)

Table 6.3. Ratio $\delta_n = A_{n-1}/A_n$ of total measure of successive collision number generations and fractal dimension d .

n	$r/R = 0.35$		$r/R = 0.6$	
	δ_n	d	δ_n	d
2	2.6426	0.4163	1.0653	0.9163
3	4.3386	0.3208	1.6135	0.5916
4	4.3275	0.3212	2.0695	0.4880
5	4.3298	0.3211	2.0634	0.4890
6	4.2903	0.3225	2.0623	0.4892
7	4.4286	0.3178	2.0618	0.4893
8	3.2667	0.3693	2.0624	0.4892
9	5.0000	0.3010	2.0603	0.4895
10			2.0858	0.4853
11			1.9593	0.5075

with $m = 2$. Table 6.3 lists the results of such a computation for $r = 6$ and $R = 10$. Data from 200 000 trajectories in an impact parameter interval $0.5 \leq b \leq 2.5$ have been used. The data for the largest values of n are unreliable, since they are based on a small number of trajectories. From the results shown in the table, we can assign a fractal dimension of $d \approx 0.321$ for $r/R = 0.35$ and $d = 0.489$ for $r/R = 6$. This can be checked by computing data from magnified intervals and higher collision numbers. The fractal dimension for $r/R = 0.35$ is in good agreement with the numerical values in Ref. [5]; fractal dimensions for larger radii are not reported there. The simple estimate (6.14) yields $d = 0.52$, which is somewhat larger than the numerical value.

Figure 6.17 compares finally the fractal dimensions calculated using the program with those of the approximate formula (6.14) and shows good overall agreement, remarkable in view of the simplicity of the approximation.

6.4.5 Suggestions for Additional Experiments

Long-Lived Trajectories: For larger disk radii, more and more trajectories get trapped for longer times. This happens, in particular, in the case of disks which almost touch each other, i.e., $r \lesssim \sqrt{3}R/2 \approx 0.866R$ for an equilateral triangular configuration. Figure 6.18 shows the scattering functions for $r = 8.5$ and $R = 10$ and a small impact parameter interval $0.22295 \leq b \leq 0.22296$ scanned by 1000 trajectories. The fractal dimension is found to be not much below unity.

One can locate an orbit with 204 impacts at an impact parameter b_ν with relative coordinate $\nu = 496$ (see (6.10)). (Due to the extreme numerical

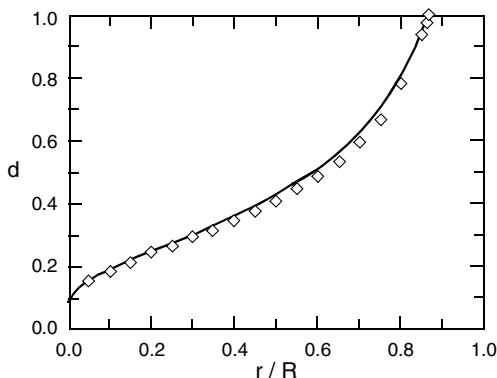


Fig. 6.17. Fractal dimension d as a function of the disk radius. Numerical results (\diamond) are compared with the estimate (6.14) (—).

instability, the computed scattering diagrams may be machine dependent in this case.) The collision sequence for this orbit is

$$\begin{aligned} & '1^4 0^3 10^3 1^2 0(01)^2 101^3 (01)^4 1^2 010^2 1^2 01^4 01^2 01^6 01^5 \\ & 01^6 (01)^2 1^2 0^4 1^2 (01)^4 0^2 1^2 (01)^7 10(01)^2 0^3 1^3 0^3 (01)^{10} \\ & 1^2 01^2 01^3 01^6 010^6 1^3 0^4 (01)^2 10^2 1^2 (01)^5 10^3 1^2 0^3 1^3 0'. \end{aligned}$$

Several sub-sequences occur in this collision sequence, where the trajectory gets close to a periodic orbit. The simple triangular orbit (1) in Fig. 6.16 appears several times (' 1^4 ', ' 0^7 ', ' 1^6 ', ' 0^7 ', ' 1^8 ', ...) and the two-bounce orbit ' 10 ', in particular, appears quite often. Here, the particle enters the small exit channel between two disks and is reflected on both sides, while energy is converted from transverse to vibrational motion until a reflection back into the interior region occurs.

Looking at Fig. 6.18, one observes characteristic smooth structures between erratic looking regions. Here, the collision sequences are also quite long, albeit highly organized. Magnifying such an interval reveals a clear sawtooth structure of the deflection function, accompanied by a staircase in the collision number. This can be understood by looking at the collision sequence, which ends up with a tail ' $\dots(01)^k$ '. This tail is an oscillation between two disks until the particle finally escapes. When the impact parameter is varied, the scattering angle changes over a large range until the trajectory becomes tangential to the other disk and an additional impact occurs. This effect is also visible in a two-disk system, where the projectile is trapped in the small channel between the two disks.

Incomplete Symbolic Dynamics: When the disk radii become larger, the disks are more and more screened by each other. This results in the fact that the one-to-one correspondence between periodic orbits and symbolic binary collision sequences is destroyed. Some of the sequences no longer appear as periodic orbits; they are 'forbidden', because otherwise the projectile would have to transverse one of the disks. One can investigate this process, find for-

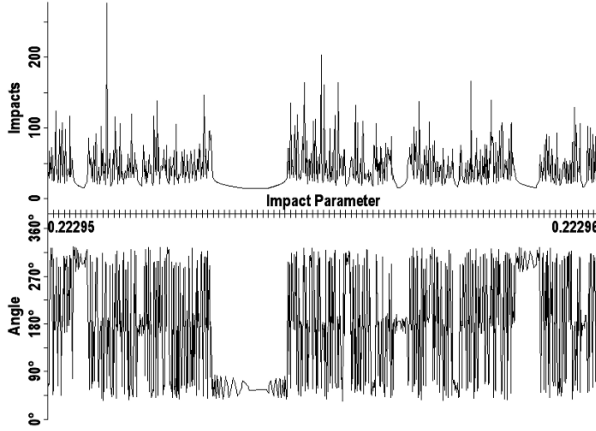


Fig. 6.18. Collision number $n(b)$ and scattering angle $\vartheta(b)$ as a function of the impact parameter b for $r = 8.5$ and $R = 10$.

bidden collision sequences, discuss the organization of the binary coding tree and study the fractal properties of such a case.

Multiscale Fractals: As discussed above, the fractals appearing in the three-disk system are not single-scale fractals. They are multi-scale fractals, as discussed, e.g., in the review article by Tél [12]. In the above examples, the scaling differences are, however, quite small. One can try to emphasize these differences by varying the disk sizes, the distances and positions of the disks and studying the fractal properties.

6.5 Suggestions for Further Studies

Chaotic scattering for smooth potentials has been studied by Jung for a potential with three maxima [14, 15]. Periodic orbit organization, Cantor set singularity structure, and the semiclassical limit of quantum scattering have been investigated.

Quantum scattering: Three-disk scattering also serves as a model for exploring chaotic phenomena in quantum scattering [4, 6, 7]. In the semiclassical limit of small wavenumbers, the scattering cross sections can be described using the Gutzwiller trace formula, which is based on the classical periodic orbits. In particular, the symbolic dynamics described above has been successfully used in such an analysis.

6.6 Real Experiments and Empirical Evidence

The chaotic reflections from a system of three shiny (Christmas-tree) balls, which is a three-dimensional version of the planar model in this case, can be studied in an everyday experiment (see Walker [16], as well as the numerical simulation by Korsch and Wagner [10]).

Berkovich et al. [8] monitored the scattered laser light from highly reflecting cylinders. Their set-up is such that a laser is positioned on a traveling microscope ($\Delta x \sim 0.1\text{mm}$) and the cylinders positioned on a plane parallel to each other; the scattering objects, mounted on this plane, can be rotated and this angle recorded. Ray-tracing is achieved using smoke, the laserspot then being scattered onto a screen. It is possible to demonstrate qualitatively the scattering pattern, measure the Lyapunov exponent and introduce the Cantor set and fractal dimensions.

References

1. B. Eckhardt, *Irregular scattering*, Physica D **33** (1988) 89
2. U. Smilansky, *The Classical and Quantum Theory of Chaotic Scattering*, in *Les-Houches Summer School on Quantum Chaos 1989*, page 371. Elsevier, Amsterdam, 1990
3. R. Blümel, *Quantum Chaotic Scattering*, in Hao Bai-Lin, D. H. Feng, and J.-M. Yuan, editors, *Directions in Chaos*. World Scientific, Singapore, 1991
4. P. Gaspard and S. A. Rice, *Scattering from a classically chaotic repeller*, J. Chem. Phys. **90** (1989) 2225
5. B. Eckhardt, *Fractal properties of scattering singularities*, J. Phys. A **20** (1987) 5971
6. P. Gaspard and S. A. Rice, *Semiclassical quantization of the scattering from a classically chaotic repeller*, J. Chem. Phys. **90** (1989) 2242
7. P. Gaspard and S. A. Rice, *Exact quantization of the scattering from a classically chaotic repeller*, J. Chem. Phys. **90** (1989) 2255
8. C. Berkovich, U. Smilansky, and G. P. Farmelo, *Demonstration of classical chaotic scattering*, Eur. J. Phys. **12** (1991) 122
9. Q. Chen, M. Ding, and E. Ott, *Chaotic scattering in several dimensions*, Phys. Lett. A **145** (1990) 93
10. H. J. Korsch and A. Wagner, *Fractal Mirror Images and Chaotic Scattering*, Computers in Physics (Sept./Oct. 1991) 497
11. J. V. José, C. Rojas, and E. J. Saletan, *Elastic particle scattering from two hard disks*, Am. J. Phys. **60** (1992) 587
12. T. Tél, *Fractals, multifractals and thermodynamics*, Z.Naturforsch. **43a** (1988) 1154
13. M. V. Berry, *Reflections on a Christmas-tree bauble*, Phys. Edu. **7** (1972) 1
14. C. Jung and H. J. Scholz, *Cantor set structure in the singularities of classical potential scattering*, J. Phys. A **20** (1987) 3607
15. C. Jung and S. Pott, *Classical cross section for chaotic potential scattering*, J. Phys. A **22** (1989) 2925; *Semiclassical cross section for a classically chaotic scattering system*, J. Phys. A **23** (1990) 3727
16. J. Walker, *The distorted images seen in Christmas-tree ornaments and other reflecting balls*, Scientific American **259** (December 1989) 84